INTERNATIONAL JOURNAL FOR NUMERICAL METHODS IN FLUIDS
*Int. J. Numer. Meth. Fluids* 2000; **32**: 745–772

# Numerical studies on non-linear free surface flow using generalized Schwarz–Christoffel transformation

J. M. Chuang*,[1]

*Department of Mechanical Engineering, Dalhousie University, PO Box 1000, Halifax, Nova Scotia, Canada B3J 2X4*

## SUMMARY

This paper deals with a technique to transform a free surface flow problem in the physical domain with an unknown boundary to a standard domain that has a fixed boundary. All the difficulties in the physical domain are reduced to finding an unknown mapping function that can be solved iteratively in a standard domain. A derivation is first presented to express an analytic function in terms of the boundary value of its imaginary part. Using a relationship between boundaries of the standard and the physical domains, a formula for the generalized Schwarz–Christoffel transformation is then developed. Based on the generalized Schwarz–Christoffel integral and the Hilbert transform, a pair of non-linear boundary integro-differential equations in an infinite strip is formulated for solving fully non-linear free surface flow problems. The boundary integral equations are then discretized with quadratic elements in an untruncated standard domain and solved by the Levenberg–Marquardt algorithm. Several examples of supercritical flow past obstructions are provided to demonstrate the flexibility and the accuracy of the proposed numerical scheme. Copyright © 2000 John Wiley & Sons, Ltd.

KEY WORDS: Green's function method; singular integral; Levenberg–Marquardt algorithm; supercritical flow

## 1. INTRODUCTION

Since the last century, free surface flow has been investigated by numerous researchers. Pioneering work can be found in Reference [1]. Owing to recent advances in the capabilities of computer systems, the fully non-linear free surface flow problems can now be tackled. The challenge associated with the solution of a fully non-linear free surface flow problem is twofold. One is that only a part of the boundaries, i.e. the solid boundary, in the physical domain is given and the other is that a non-linear free surface condition, derived from the Bernoulli equation, has to be imposed on an unknown boundary of the free surface. Furthermore, from a computational point of view, the numerical computation in an

* Correspondence to: Department of Mechanical Engineering, Dalhousie University, PO Box 1000, Halifax, Nova Scotia, Canada B3J 2X4.
[1] E-mail: jimmy.chuang@dal.ca

*Received 25 September 1998*
*Revised 28 April 1999*

untruncated infinite domain with the involvement of the singular integrals is a source of headache for the researchers. It is noted that the boundary integral equation method formulated in the physical domain is not directly applicable to this kind of problem. It is mainly due to the fact that the boundary integral equation method is based on a given geometry of the physical domain. If a part of the boundary in the physical domain is not known, the solution, which entirely depends on the boundary, has to be determined using a trial and error approach, such as

1. guessing the unknown part of the boundary as well as the boundary condition;
2. solving the boundary integral equation;
3. checking the boundary condition on the unknown part of the boundary;
4. based on the difference of the boundary condition on the unknown part of the boundary, guessing a new boundary;
5. repeating the whole process and hoping that eventually the unknown part of the boundary and the solution will converge.

This interesting topic has been studied intensively in several types of physical problems, such as the free surface flow over a polygonal obstacle [2–7], over a step [8], over a semi-circular obstruction [9,10], as well as a waterfall [11–15]. Some other applications in the engineering field can be found in References [16–21]. Most of these studies are based on a conformal mapping technique, which maps a variety of standard domains, such as an upper-half plane [2,6,14,19], a unit disk [16], the upper-half of a unit disk [7,18,19] and an infinite strip [4,8], onto the physical domain with an unknown boundary. The special features of this technique are

1. The non-linear free surface condition can be transformed analytically and applied to a fixed boundary in the standard domain. This is because the unknown free surface in the physical domain can be represented by the mapping function in the standard domain.
2. The unknown mapping function in the standard domain is expressed in terms of the complex velocity in the physical domain through a relationship between the boundaries of the physical and standard domains. Once the mapping function is solved, the solution for the fully non-linear free surface flow problem can be found.
3. No approximation of the boundary in the standard domain is necessary in the numerical computation of the boundary integral equations and the computation can be carried out in an untruncated standard domain under certain assumption.

The theory behind this kind of conformal mapping, in fact, is the so-called generalized Schwarz–Christoffel transformation [22,23], which is an inverse mapping, i.e. mapping a standard domain onto a physical domain, and has to be solved iteratively. Consequently, there are two levels of iterations involved in the numerical solution of the non-linear free surface flow. One being the iterations for satisfying the non-linear free surface condition in the standard domain and the other the inverse mapping for satisfying the geometry of the solid boundary in the physical domain, such as the bottom shape of a free surface flow over an obstruction.

In this paper, Section 2 deals with the generalized Schwarz–Christoffel transformation with an application to map an upper-half plane onto an elongated channel with infinite length, such

 

as the configuration of the flow past an obstacle or a water fall in the physical domain. In Section 3, a discussion of the formulation of the boundary integral equations for solving a fully non-linear free surface flow problem in the standard domain of the infinite strip is presented. The techniques for discretizing the boundary integral equations, numerical treatment of the non-linear free surface condition with both integral and differential methods, and a two-level iteration scheme for obtaining a converged solution of the non-linear, free surface flow problem are introduced in Section 4. To demonstrate the accuracy and efficiency of this numerical scheme, Section 5 presents the computational results of supercritical flow past a triangular obstruction with different heights and a ramp with different heights and angles. The detailed numerical treatment of the singular integrals involved in the discretized boundary integral equations is also included in Appendix A.

## 2. GENERALIZED SCHWARZ–CHRISTOFFEL TRANSFORMATION

This section summarizes the generalized Schwarz–Christoffel transformation for mapping an arbitrary standard domain onto an arbitrary physical domain [23]. It is based on the boundary integral expression of an analytic function, a relationship between the boundaries of the physical and standard domains and the Green's function of the first and the second kinds for the physical domain. The formula is then applied to a special standard domain, namely, an upper-half plane.

### *2.1. Arbitrary standard domain*

Assume that the physical domain $R_z$, bounded by the curve $s_z$, and the corresponding standard domain $R_\zeta$, surrounded by the curve $s_\zeta$, are on the $z$- and $\zeta$-plane respectively.

The mapping function, $z(\zeta)$, which maps an arbitrary standard domain onto an arbitrary physical domain, is given by [23]

$$\frac{\mathrm{d}z}{\mathrm{d}\zeta} = D_1 \, \mathrm{e}^{f(\zeta)} \quad \text{or} \quad z(\zeta) = D_1 \int^{\zeta} \mathrm{e}^{f(\zeta_0)} \, \mathrm{d}\zeta_0 + D_2 \tag{1}$$

where $D_1$ and $D_2$ are arbitrary constants.

The auxiliary function $f(\zeta)$ in Equation (1) is defined as

$$\begin{aligned} f(\zeta) = & -\{G^{(2)}(P, Q)[\bar{\theta}(Q) - \theta_\zeta(Q)]\}_{Q_s}^{Q_e} \\ & + \int_{s_\zeta} [\bar{\theta}(Q) - \theta_\zeta(Q)] \left\{ \frac{\partial G^{(2)}(P, Q)}{\partial s_Q} + \mathrm{i} \frac{\partial G^{(1)}(P, Q)}{\partial n_Q} \right\} \mathrm{d}s_Q + C \end{aligned} \tag{2}$$

where $G^{(1)}$ and $G^{(2)}$ are Green's function of the first and second kind of the physical domain $R_z$, and $\bar{\theta} = \theta_z(s_z(s_\zeta))$ and $\theta_\zeta$ are tangent angles at the corresponding point on the boundary $s_z$ and $s_\zeta$ respectively.

 

### 2.2. Standard domain of an upper-half plane

Let the standard domain $R_\zeta$ be an upper-half plane. It is clear that the boundary $s_\zeta$ of the domain includes the $\xi$-axis and the boundary $s_\sigma$ of a semi-circle with a sufficiently large radius $R$. Green's functions of the first and second kinds for this domain are

$$G^{(1)}(\xi_0, \eta_0;\ \xi, \eta) = \frac{1}{2\pi}\{\log\sqrt{(\xi_0-\xi)^2+(\eta_0-\eta)^2} - \log\sqrt{(\xi_0-\xi)^2+(\eta_0+\eta)^2}\} \tag{3}$$

$$G^{(2)}(\xi_0, \eta_0;\ \xi, \eta) = \frac{1}{2\pi}\{\log\sqrt{(\xi_0-\xi)^2+(\eta_0-\eta)^2} + \log\sqrt{(\xi_0-\xi)^2+(\eta_0+\eta)^2}\} \tag{4}$$

Substituting Equation (4) into Equation (2) gives the auxiliary function for mapping an upper-half plane onto an arbitrary physical domain,

$$f(\zeta) = -\frac{1}{\pi}\left\{[\bar{\theta}(\xi)\log\sqrt{(\xi_0-\xi)^2+\eta^2}]_{-\infty}^{\infty} + \int_{-\infty}^{\infty}\frac{\bar{\theta}(\xi)}{\zeta-\xi}\,\mathrm{d}\xi\right\} + C \tag{5}$$

If the physical domain is an upper-half plane bounded by a curved boundary and $\theta_z = 0$ as $x \to \pm\infty$, then the auxiliary function $f(\zeta)$ reduces to

$$f(\zeta) = -\frac{1}{\pi}\int_{-\infty}^{\infty}\frac{\bar{\theta}(\xi)}{\zeta-\xi}\,\mathrm{d}\xi + C \tag{6}$$

On the other hand, if the contour of the physical domain is an infinite strip with a curved boundary (see Figure 1), four points, $a$, $b$, $c$ and $d$ at $x \to \infty$, may be selected that correspond to $\xi_a$, $\xi_b$, $\xi_c$ and $\xi_d$ on the $\xi$-axis in the standard domain ($\zeta$-plane). Let $\theta_1$, $\theta_2$ and $\theta_3$ be tangential angles along the segments $\overline{ab}$, $\overline{bc}$ and $\overline{cd}$ in the physical domain respectively. Since $\theta_1$, $\theta_2$ and $\theta_3$ are constant (in fact, they are 0, $\pi/2$ and $\pi$), the auxiliary function $f(\zeta)$ is written as

$$\begin{aligned} f(\zeta) &= -\frac{1}{\pi}\left\{\int_{-i}^{\xi_a}\frac{\bar{\theta}(\xi)}{\zeta-\xi}\,\mathrm{d}\xi + \theta_1\int_{\xi_a}^{\xi_b}\frac{1}{\zeta-\xi}\,\mathrm{d}\xi + \theta_2\int_{\xi_b}^{\xi_c}\frac{1}{\zeta-\xi}\,\mathrm{d}\xi + \theta_3\int_{\xi_c}^{\xi_d}\frac{1}{\zeta-\xi}\,\mathrm{d}\xi \right.\\ &\quad \left. + \int_{\xi_d}^{\infty}\frac{\bar{\theta}(\xi)}{\zeta-\xi}\,\mathrm{d}\xi\right\} + C \\ &= -\frac{1}{\pi}\left\{\int_{-\infty}^{\xi_a}\frac{\bar{\theta}(\xi)}{\zeta-\xi}\,\mathrm{d}\xi + \frac{\pi}{2}\log(\zeta-\xi_b) + \frac{\pi}{2}\log(\zeta-\xi_c) + \int_{\xi_d}^{\infty}\frac{\bar{\theta}(\xi)}{\zeta-\xi}\,\mathrm{d}\xi\right\} + C \end{aligned} \tag{7}$$

As points $b$ and $c$ in the physical domain tend to infinity, the corresponding points $\xi_b$ and $\xi_c$ in the $\zeta$-plane will approach 0. The auxiliary function $f(\zeta)$ is thus reduced to

$$f(\zeta) = -\log\zeta - \frac{1}{\pi}\left\{\int_{-\infty}^{\infty}\frac{\bar{\theta}(\xi)}{\zeta-\xi}\,\mathrm{d}\xi\right\} + C \tag{8}$$

 

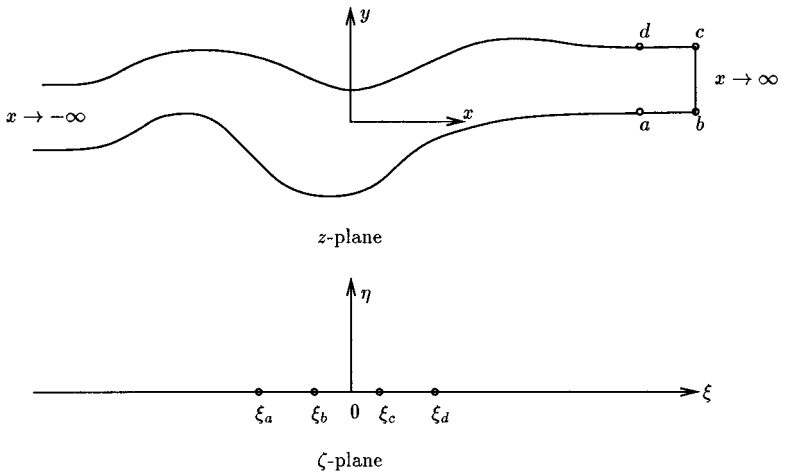


Figure 1. Mapping of an elongated channel.

Consequently, the generalized Schwarz–Christoffel transformation, which maps the upper-half of the $\xi$-plane to an elongated channel with infinite length in the $z$-plane, is expressed as

$$\frac{\mathrm{d}z}{\mathrm{d}\zeta} = -\frac{1}{\pi\zeta}\exp\left\{-\frac{1}{\pi}\int_{-\infty}^{\infty}\frac{\bar{\theta}(\xi)}{\zeta-\xi}\,\mathrm{d}\xi\right\}$$

or

$$z(\zeta) = -\int^{\zeta}\frac{1}{\pi\zeta_0}\exp\left\{-\frac{1}{\pi}\int_{-\infty}^{\infty}\frac{\bar{\theta}(\xi)}{\zeta_0-\xi}\,\mathrm{d}\xi\right\}\mathrm{d}\zeta_0 + D_2 \tag{9}$$

As the field point $\zeta$ approaches the $\xi$-axis, the integral in Equation (9) becomes a Cauchy-type integral,

$$z(\xi) = -\int_{-\infty}^{\xi}\frac{1}{\pi s}\exp\left\{-\frac{1}{\pi}\int_{-\infty}^{\infty}\frac{\bar{\theta}(t)}{s-t}\,\mathrm{d}t + \mathrm{i}\bar{\theta}(s)\right\}\mathrm{d}s + D_2 \tag{10}$$

## 3. FORMULATION OF THE FREE SURFACE FLOW PROBLEM

For simplicity, consider a free surface flow past an obstacle as shown in Figure 2.

It is assumed that the fluid is inviscid and incompressible, and the flow is irrotational and steady. Far upstream, the depth and the velocity of the flow are $h$ and $U_0$ respectively. The gravity is acting in the $-Y$-direction. The mathematical problem is to find a complex potential, $F(X, Y) = \phi(X, Y) + \mathrm{i}\psi(X, Y)$, satisfying the following boundary conditions in the $z$-plane:

 

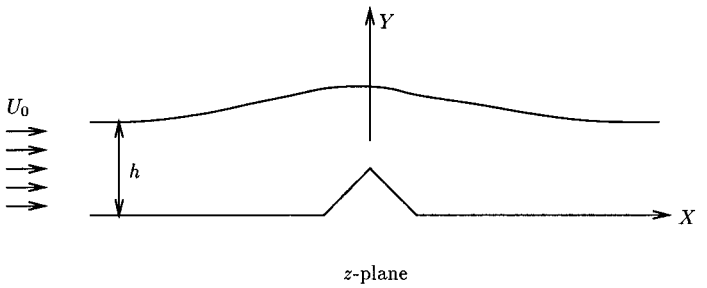


Figure 2. Free surface flow past an obstacle.

1. On the solid boundary (bottom), fluid particles cannot penetrate the surface, i.e.

$$\frac{\partial \phi}{\partial n} = 0 \quad \text{or} \quad \psi = \text{constant} \tag{11}$$

where $\vec{n}$ is the normal of the bottom surface.

2. On the free surface, the Bernoulli equation has to be satisfied

$$\frac{P_a}{\rho} + \frac{1}{2} Q^2 + gY = \text{constant} = \frac{P_a}{\rho} + \frac{1}{2} U_0^2 + gh \tag{12}$$

where $P_a$ is the atmospheric pressure, $\rho$ is the density, $g$ is the gravitational constant and $Q^2 = u^2 + v^2$ is the magnitude of the velocity $\vec{V}$ of a fluid particle. It is noted that the right-hand-side of Equation (12) is evaluated at the free surface far upstream.

Choosing $h$ and $U_0$ as the reference length and velocity, and introducing the non-dimensional variables shown in Equation (13),

$$p = \frac{P}{\rho U_0^2}; \qquad q = \frac{Q}{U_0}; \qquad y = \frac{Y}{h} \tag{13}$$

the free surface condition (12) reduces to

$$q^2 + \frac{2}{F_n^2}(y - 1) = 1 \quad \text{on the free surface} \tag{14}$$

where $F_n = U_0^2/\sqrt{gh}$ is the depth Froude number and the pressure, $P_a$, on the free surface is assumed to be zero.

It is noted that if the magnitude $q(x, y)$ of the non-dimensional velocity is known, then the non-dimensional pressure $p(x, y)$, i.e. the pressure coefficient, can be evaluated from

 

$$p(x, y) = \frac{1}{2}[1 - q(x, y)^2] + \frac{1}{F_n^2}(1 - y) \tag{15}$$

### 3.1. Formulation of the integral equation

If the upper half of the $\zeta$-plane is chosen to be a standard domain, the complex potential $\bar{F}(\zeta)$ due to a sink located at $\zeta = 0$ is given by

$$\bar{F}(\zeta) = -\frac{1}{\pi}\log\zeta = \phi(\xi, \eta) + \mathrm{i}\psi(\xi, \eta) \tag{16}$$

Using the chain rule and the generalized Schwarz–Christoffel formula shown in Equation (10), the complex velocity in the $z$-plane can be expressed as

$$W(z) = \frac{\mathrm{d}F}{\mathrm{d}z} = \frac{\mathrm{d}\bar{F}}{\mathrm{d}\zeta}\frac{\mathrm{d}\zeta}{\mathrm{d}z} = \exp\left\{\frac{1}{\pi}\int_{-\infty}^{\infty}\frac{\bar{\theta}(t)}{\zeta - t}\,\mathrm{d}t\right\} \tag{17}$$

Furthermore, the complex velocity $W(z)$ can also be expressed in terms of the velocity components, $u$ and $v$, in the $z$-plane,

$$W(z) = u(x, y) + \mathrm{i}v(x, y) = q(x, y)\,\mathrm{e}^{-\mathrm{i}\theta(x,y)} \tag{18}$$

where $q = \sqrt{u^2 + v^2}$ and $\theta = \tan^{-1}(u/v)$.

By combining Equations (17) and (18), and letting the field point $\zeta$ in Equation (17) approach the real $\xi$-axis in the $\zeta$-plane, you obtain

$$W(z(\zeta))\big|_{\zeta\to\xi} = \left\{\frac{\mathrm{d}\bar{F}}{\mathrm{d}\zeta}\frac{\mathrm{d}\zeta}{\mathrm{d}z}\right\}_{\zeta\to\xi} = \exp\left\{\frac{1}{\pi}\int_{-\infty}^{\infty}\frac{\bar{\theta}(t)}{\zeta - t}\,\mathrm{d}t - \mathrm{i}\bar{\theta}(\xi)\right\} = \bar{q}(\xi)\,\mathrm{e}^{-\mathrm{i}\bar{\theta}(\xi)} \tag{19}$$

where $\bar{q}(\xi) = q(x(\xi, 0), y(\xi, 0))$.

By taking the log of Equation (19), you finally arrive at

$$\bar{p}(\xi) = -\log\bar{q}(\xi) = -\frac{1}{\pi}\int_{-\infty}^{\infty}\frac{\bar{\theta}(t)}{\xi - t}\,\mathrm{d}t \tag{20}$$

As a result, the mapping function $z(\xi)$, which maps the boundary in the $\zeta$-plane to that in the $z$-plane, can be simply expressed in terms of $\bar{q}(\xi)$ and $\bar{\theta}(\xi)$,

$$z(\xi) = -\int_{\infty}^{\xi}\frac{1}{\pi s}\bar{q}(s)^{-1}\,\mathrm{e}^{\mathrm{i}\bar{\theta}(s)}\,\mathrm{d}s \tag{21}$$

It also gives a simple expression for $\mathrm{d}x/\mathrm{d}\xi$ and $\mathrm{d}y/\mathrm{d}\xi$,

$$\frac{\mathrm{d}x}{\mathrm{d}\xi} = -\frac{1}{\pi\xi}\frac{\cos\bar{\theta}(\xi)}{\bar{q}(\xi)}, \qquad \frac{\mathrm{d}y}{\mathrm{d}\xi} = -\frac{1}{\pi\xi}\frac{\sin\bar{\theta}(\xi)}{\bar{q}(\xi)} \tag{22}$$

 

Instead of solving the mapping function $z(\zeta)$ directly, an analytic function $H(\zeta)$ in the $\zeta$-plane, which is composed of two real functions, $\bar{p}(\zeta) = -\log \bar{q}(\zeta)$ and $\bar{\theta}(\zeta)$, may be defined as follows [2]:

$$H(\zeta) = \frac{\bar{p}(\zeta) + \mathrm{i}\bar{\theta}(\zeta)}{\mathrm{i}\sqrt{\zeta}} \tag{23}$$

Applying the Hilbert transform, which expresses the real part of an analytic function in terms of the imaginary part and vice versa, to function $H$, a set of integral equations is then obtained

$$\bar{p}(\xi_b) = \frac{1}{\pi}\left\{\int_{-\infty}^{0} \sqrt{\frac{-\xi_b}{-t_b}}\,\frac{\bar{\theta}(t_b)}{\xi_b - t_b}\,\mathrm{d}t_b + \int_{0}^{\infty} \sqrt{\frac{-\xi_b}{t_f}}\,\frac{\bar{p}(t_f)}{\xi_b - t_f}\,\mathrm{d}t_f\right\} \quad \text{for } \xi_b < 0 \tag{24}$$

$$\bar{\theta}(\xi_f) = -\frac{1}{\pi}\left\{\int_{-\infty}^{0} \sqrt{\frac{\xi_f}{-t_b}}\,\frac{\bar{\theta}(t_b)}{\xi_f - t_b}\,\mathrm{d}t_b + \int_{0}^{\infty} \sqrt{\frac{-\xi_f}{t_f}}\,\frac{\bar{p}(t_f)}{\xi_f - t_f}\,\mathrm{d}t_f\right\} \quad \text{for } \xi_f > 0 \tag{25}$$

In the above equations, $\xi_b$ and $\xi_f$ are used for denoting $-\infty < \xi < 0$ and $0 < \xi < \infty$, as shown in Figure 3.

To avoid the difficulties caused by the singular point $\zeta = 0$ in the $\zeta$-plane and maintain an untruncated boundary in the standard domain for the numerical computation, this pair of integral equations can be further transformed to an infinite strip in the $\bar{F}$-plane with the mapping function

$$\bar{F}(\zeta) = -\frac{1}{\pi}\log\zeta = \phi(\zeta) + \mathrm{i}\psi(\zeta) \tag{26}$$

Consequently, the integral equations (24) and (25) are transformed to

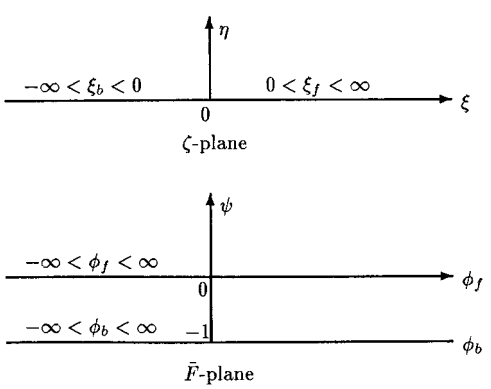


Figure 3. Boundaries in $x$- and $\bar{F}$-plane.

 

$$\tilde{p}(\phi_b) = -\int_{-\infty}^{\infty} \frac{\tilde{\theta}(s_b)}{2\sinh\frac{\pi}{2}(\phi_b - s_b)}\,\mathrm{d}s_b + \int_{-\infty}^{\infty} \frac{\tilde{p}(s_f)}{2\cosh\frac{\pi}{2}(\phi_b - s_f)}\,\mathrm{d}s_f, \quad \text{for } -\infty < \phi_b < \infty \tag{27}$$

$$\tilde{\theta}(\phi_f) = \int_{-\infty}^{\infty} \frac{\tilde{\theta}(s_b)}{2\cosh\frac{\pi}{2}(\phi_f - s_b)}\,\mathrm{d}s_b - \int_{-\infty}^{\infty} \frac{\tilde{p}(s_f)}{2\sinh\frac{\pi}{2}(\phi_f - s_f)}\,\mathrm{d}s_f, \quad \text{for } -\infty < \phi_f < \infty \tag{28}$$

### *3.2. Formulation of the free surface conditions*

Differentiating the free surface condition shown in Equation (14) with respect to $\xi$ gives

$$F_n^2 \bar{q}\frac{\mathrm{d}\bar{q}}{\mathrm{d}\xi} + \frac{\mathrm{d}y}{\mathrm{d}\xi} = 0 \tag{29}$$

Substituting Equation (22) into Equation (29), integrating with respect to $\xi$ and transforming to the $\bar{F}$-plane, the integral form of the free surface condition in the $\bar{F}$-plane is thus obtained,

$$\tilde{p}(\phi_f) = -\log\tilde{q}(\phi_f) = -\frac{1}{3}\log\left\{1 - \frac{3}{F_n^2}\int_{-\infty}^{\phi_f} \sin\tilde{\theta}(s_f)\,\mathrm{d}s_f\right\} \tag{30}$$

where $\phi_f$ is along the top part of the straight channel as shown in Figure 3.

Based on the integral form of the free surface condition (30), it is not difficult to derive the differential form of the free surface condition in the $\bar{F}$-plane,

$$\frac{\mathrm{d}\tilde{p}}{\mathrm{d}\phi_f} = \frac{1}{F_n^2}\,\mathrm{e}^{3\tilde{p}(\phi_f)}\sin\tilde{\theta}(\phi_f) \tag{31}$$

## 4. NUMERICAL COMPUTATION

In this section, the bottom of the physical domain ($z$-plane) is assumed to have a polygonal surface, so that the first integral in Equation (27) can be carried out analytically. Section 4.1 presents a method to maintain an untruncated domain in the numerical computation. The standard domain, i.e. an infinite strip in the $\bar{F}$-plane, is divided into three regions, up, mid and downstream. The unknown functions $\tilde{p}$ and $\tilde{\theta}$ in the upstream (downstream) are assumed to be constants, which are identical to their numerical values at the first (last) grid point in the midstream. Consequently, only a portion of the integral equation has to be discretized.

A two-level iteration scheme, i.e.

1. the numerical treatment of the non-linear free surface condition in the standard domain, and

 

2. the inverse mapping of the generalized Schwarz–Christoffel transformation for the bottom geometry,

to obtain a converged solution for the free surface flow past a polygonal bottom surface is described in detail in Section 4.2.

### *4.1. Discretization of integral equation*

Consider a free surface flow past an obstacle with a polygonal surface as shown in Figure 4.

The integral equation to be solved is given by Equation (27), in which the first integral only relates the bottom shape. If the shape of the polygonal bottom is given and the corresponding points (in the $\bar{F}$-plane) to the vertices of the bottom in the physical domain ($z$-plane) are assumed, this integral can be carried out analytically,

$$\int_{-\infty}^{\infty} \frac{\tilde{\theta}(s_b)}{2\cosh\dfrac{\pi}{2}(\phi_f - s_b)}\,\mathrm{d}s_b = -\frac{1}{\pi}\sum_{i=1}^{N_\alpha - 1}(\alpha_{i+1}-\alpha_i)\tan^{-1}\left[\sin\frac{\pi}{2}(\phi_f - s_{b_i})\right] \tag{32}$$

The second integral in Equation (28) can be divided into three parts based on the variation of the velocity in the up, mid and downstreams, as shown in Figure 5, with an assumption of no waves propagating downstream

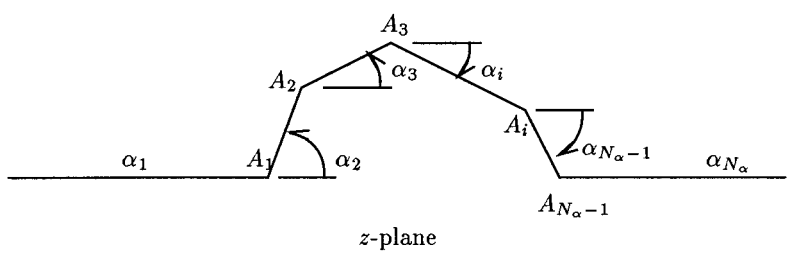


Figure 4. Obstacle with polygonal surface.

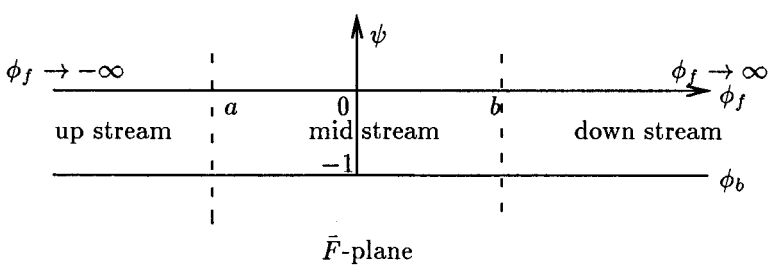


Figure 5. Up, mid and downstream in the $\bar{F}$-plane.

 

$$-\int_{-\infty}^{\infty} \frac{\tilde{p}(s_f)}{2\sinh\frac{\pi}{2}(\phi_f - s_f)}\,\mathrm{d}s_f = -\int_{-\infty}^{a} \frac{\tilde{p}(s_f)}{2\sinh\frac{\pi}{2}(\phi_f - s_f)}\,\mathrm{d}s_f - \int_{a}^{b} \frac{\tilde{p}(s_f)}{2\sinh\frac{\pi}{2}(\phi_f - s_f)}\,\mathrm{d}s_f - \int_{b}^{-\infty} \frac{\tilde{p}(s_f)}{2\sinh\frac{\pi}{2}(\phi_f - s_f)}\,\mathrm{d}s_f \tag{33}$$

Using the quadratic elements to discretize the free surface in the midstream ($a < \phi_f < b$) into $N$ elements, the second integral is then approximated by

$$-\int_{-\infty}^{\infty} \frac{\tilde{p}(s_f)}{2\sinh\frac{\pi}{2}(\phi_f - s_f)}\,\mathrm{d}s_f = -\int_{-\infty}^{a} \frac{\tilde{p}^*_{1,1}}{2\sinh\frac{\pi}{2}(\phi_f - s_f)}\,\mathrm{d}s_f - \sum_{j=1}^{N} \int_{s_{f_j}}^{s_{f_{j+1}}} \frac{\sum_{k=1}^{3} \tilde{p}^*_{j,k} N_k(\gamma(s_f))}{2\sinh\frac{\pi}{2}(\phi_f - s_f)}\,\mathrm{d}s_f - \int_{b}^{-\infty} \frac{\tilde{p}^*_{N-1,3}}{2\sinh\frac{\pi}{2}(\phi_f - s_f)}\,\mathrm{d}s_f \tag{34}$$

where $\tilde{p}^*_{j,k}$ is the numerical value of the function $\tilde{p}$ at the node $k$ in element $j$ and $N_k(\gamma(s_f))$, $k = 1, 2, 3$, are shape functions of the quadratic element shown below,

$$N_1(\gamma) = \frac{1}{2}\gamma(\gamma - 1), \qquad N_2(\gamma) = 1 - \gamma^2, \qquad N_3(\gamma) = \frac{1}{2}\gamma(\gamma + 1) \tag{35}$$

where

$$\gamma(s_f) = 2\frac{s_f - s_{f_i}}{s_{f_{i+1}} - s_{f_i}} - 1$$

It is noted that there are three nodes in each quadratic element.

Substituting Equations (32) and (34) into Equation (28) leads to a set of relationships between the tangential angles, $\tilde{\theta}^f_i$, and the log of the magnitudes of the velocities, $\tilde{p}^f_i$, at the grid points on the free surface

$$\tilde{\theta}^f_i = c_i + \sum_{j=1}^{2N+1} g_{ij}\tilde{p}^f_j, \quad \text{for } i = 1, 2, 3, \ldots, 2N+1 \tag{36}$$

where

$$c_i = -\frac{1}{\pi}\sum_{k=1}^{N_\alpha - 1} (\alpha_{k+1} - \alpha_k)\tan^{-1}\left[\sinh\frac{\pi}{2}(\phi_{f_i} - s_{b_k})\right]$$

 

and

$$g_{i,1} = -\int_{-\infty}^{a} \frac{1}{2\sinh\dfrac{\pi}{2}(\phi_{f_i}-s_f)}\,\mathrm{d}s_f - \int_{s_{f_1}}^{s_{f_2}} \frac{N_1(\gamma(s_f))}{2\sinh\dfrac{\pi}{2}(\phi_{f_i}-s_f)}\,\mathrm{d}s_f$$

$$g_{i,2j+1} = -\int_{s_{f_j}}^{s_{f_{j+1}}} \frac{N_3(\gamma(s_f))}{2\sinh\dfrac{\pi}{2}(\phi_{f_i}-s_f)}\,\mathrm{d}s_f - \int_{s_{f_{j+1}}}^{s_{f_{j+2}}} \frac{N_1(\gamma(s_f))}{2\sinh\dfrac{\pi}{2}(\phi_{f_i}-s_f)}\,\mathrm{d}s_f,$$

$$\text{for } j = 1, 2, \ldots, N-1$$

$$g_{i,2j} = -\int_{s_{f_j}}^{s_{f_{j+1}}} \frac{N_2(\gamma(s_f))}{2\sinh\dfrac{\pi}{2}(\phi_{f_i}-s_f)}\,\mathrm{d}s_f, \quad \text{for } j = 1, 2, \ldots, N$$

$$g_{i,2N+1} = -\int_{s_{f_N}}^{s_{f_{N+1}}} \frac{N_3(\gamma(s_f))}{2\sinh\dfrac{\pi}{2}(\phi_{f_i}-s_f)}\,\mathrm{d}s_f - \int_{s_{f_{N+1}}}^{\infty} \frac{1}{2\sinh\dfrac{\pi}{2}(\phi_i-s_f)}\,\mathrm{d}s_f$$

It is clear that the diagonal terms, $g(i,j)$, in the $g$ matrix involve singular integrals. A detailed procedure to remove the singularity from these integrals in the numerical computation is described in Appendix A.

### *4.2. Iteration method*

This section describes a two-level iteration scheme to solve non-linear free surface flow. In Section 4.2.1, it is assumed that the corresponding points, $a_1, a_2, \ldots, a_{N_\alpha-1}$, on the $\phi_b$-axis in the $\bar{F}$-plane to the vertices, $A_1, A_2, \ldots, A_{N_\alpha-1}$, of the polygonal surface at the bottom of the physical domain ($z$-plane) are given so that the first integral in Equation (28) can be carried out analytically. Based on Equation (30) and the shape functions used by the function $\tilde{\theta}$ on the free surface, the integral method is a straightforward numerical integration. The differential method that is based on Equation (31) is more sophisticated. The Taylor series expansion method is employed in this numerical scheme to obtain a highly accurate numerical solution for Equation (31) with a truncation error of $O(\Delta\phi_f^6)$ and can be extended to obtain a numerical solution of any order. After a converged solution is obtained for Equation (28) with the Levenberg–Marquardt algorithm [24], an iteration method is proposed in Section 4.2.2 to compute the vertices $A'_1, A'_2, \ldots, A_{N_\alpha-1}$ of the bottom surface in the physical domain through the mapping function to match the given vertices $A_1, A_2, \ldots, A_{N_\alpha-1}$.

*4.2.1. Free surface*. It is seen that there are $2N+1$ equations in Equation (36) to express the relationships of $2\times(2N+1)$ unknowns ($2N+1$ $\tilde{\theta}^f$s and $2N+1$ $\tilde{p}^f$s) at the grid points on the free surface in the standard domain. Consequently, $2N+1$ non-linear equations can be established

 

$$I_i(\tilde{\theta}^f_1, \tilde{\theta}^f_2, \ldots, \tilde{\theta}^f_{2N+1}) = \tilde{\theta}^f_i - c_i - \sum_{j=1}^{2N+1} g_{ij}\tilde{p}^f_j = 0 \quad \text{for } i = 1, 2, \ldots, 2N+1 \tag{37}$$

To solve $2 \times (2N+1)$ unknowns, another set of $2N+1$ equations has to be obtained from the transformed free surface condition, Equation (30) or (31), which is a non-linear relationship between $\tilde{\theta}$ and $\tilde{p}$ at each grid point on the free surface. The first derivative of $\tilde{p}$ with respect to $\tilde{\theta}$ required in the process of solving the non-linear equations can be obtained with the chain rule

$$\frac{\mathrm{d}\tilde{p}}{\mathrm{d}\tilde{\theta}} = \frac{\mathrm{d}\tilde{p}}{\mathrm{d}\phi_f} \Big/ \frac{\mathrm{d}\tilde{\theta}}{\mathrm{d}\phi_f} \tag{38}$$

To compute $\mathrm{d}\tilde{p}/\mathrm{d}\phi_f$ in Equation (38), the numerical value of $\tilde{p}$ at each grid point is required. It can be obtained by two different approaches.

**1. Integral method** (based on Equation (30))
Since in element $k$, the function $\tilde{\theta}$ is approximated by $\tilde{\theta}^f_{2k-1}N_1(\phi_f) + \tilde{\theta}^f_{2k}N_2(\phi_f) + \tilde{\theta}^f_{2k+1}N_3(\phi_f)$, the integral form of the free surface condition, Equation (30), can be carried out numerically by

$$\begin{aligned}
\tilde{p}^f_{2i+1} = & -\frac{1}{3}\log\left\{1 - \frac{3}{F_n^2}\sum_{k=1}^{i}\int_{\phi_{f_k}}^{\phi f_{k+1}} \sin[\tilde{\theta}^f_{2k-1}N_1(\phi_f) + \tilde{\theta}^f_{2k}N_2(\phi_f) + \tilde{\theta}^f_{2k+1}N_3(\phi_f)]\,\mathrm{d}\phi_f\right\} \\
\tilde{p}^f_{2i} = & -\frac{1}{3}\log\left\{1 - \frac{3}{F_n^2}\sum_{k=1}^{i-1}\int_{\phi_{f_k}}^{\phi_{f_{k+1}}} \sin[\tilde{\theta}^f_{2k-1}N_1(\phi_f) + \tilde{\theta}^f_{2k}N_2(\phi_f) + \tilde{\theta}^f_{2k+1}N_3(\phi_f)]\,\mathrm{d}\phi_f \right. \\
& \left. - \frac{3}{F_n^2}\int_{\phi_{f_i}}^{\phi_f^*} [\tilde{\theta}^f_{2i-1}N_1(\phi_f) + \tilde{\theta}^f_{2i}N_2(\phi_f) + \tilde{\theta}^f_{2i+1}N_3(\phi_f)]\,\mathrm{d}\phi_f\right\}
\end{aligned} \tag{39}$$

where $i = 1, 2, \ldots, N$, $\phi_f^* = (\phi_{f_i} + \phi_{f_{i+1}})$and $\tilde{p}^f_1 = 0$, which is equivalent to assuming that far upstream, the velocity is unity.

**2. Differential method** (based on Equation (31))
The differential form of the free surface condition shown in Equation (31) is a first-order ordinary differential equation (ODE) with an initial condition of $\tilde{p}(-\infty)$. It can be solved by the finite difference method. However, to obtain a more accurate solution, the Taylor series expansion method up to fifth-order accuracy is adopted in this numerical scheme. For simplicity, the superscript '$f$' is neglected from the variables $\tilde{\theta}^f$ and $\tilde{p}^f$ in the following derivations.

An approximate solution of Equation (31) can be written as

$$\begin{aligned}
\tilde{p}(\phi_f + \Delta\phi_f) = & \tilde{p}(\phi_f) + \frac{\Delta\phi_f}{1!}\tilde{p}'(\phi_f) + \frac{\Delta\phi_f^2}{2!}\tilde{p}''(\phi_f) + \frac{\Delta\phi_f^3}{3!}\tilde{p}'''(\phi_f) + \frac{\Delta\phi_f^4}{4!}\tilde{p}^{\mathrm{iv}}(\phi_f) + \frac{\Delta\phi_f^5}{5!}\tilde{p}^{\mathrm{v}}(\phi_f) \\
& + O(\Delta\phi_f^6)
\end{aligned} \tag{40}$$

The derivatives of $\tilde{p}$ with respect to $\phi_f$ can be derived straightforward from Equation (31),

$$\tilde{p}' = p_1, \quad \tilde{p}'' = 3\tilde{p}' + \tilde{\theta}' p_2, \quad \tilde{p}''' = 6\tilde{p}'\tilde{p}'' + p_3 p_4 - \tilde{\theta}'^2 \tilde{p}',$$

$$\tilde{p}^{\mathrm{iv}} = 6\tilde{p}''^2 + 6\tilde{p}'\tilde{p}''' + p_4 p_5 + p_3 p_6 - 2\tilde{\theta}'\theta''\tilde{p}' - \tilde{\theta}'^2\tilde{p}''.$$

$$\tilde{p}^{\mathrm{v}} = 12\tilde{p}''\tilde{p}''' + p_7 + p_4 p_8 + 2p_5 p_6 + p_3 p_9 + p_{10} \tag{41}$$

where

$$p_1 = \frac{1}{F_n^2}\mathrm{e}^{3\tilde{p}} \sin\tilde{\theta}, \quad p_2 = \frac{1}{F_n^2}\mathrm{e}^{3\tilde{p}} \cos\tilde{\theta}, \quad p_3 = (\tilde{p}'' - 3\tilde{p}'^2), \quad p_4 = 3\tilde{p}' + \frac{\tilde{\theta}''}{\tilde{\theta}'},$$

$$p_5 = \tilde{p}''' - 6\tilde{p}'\tilde{p}'', \quad p_6 = 3\tilde{p}'' - \frac{\tilde{\theta}''^2}{\tilde{\theta}'^2}, \quad p_7 = 6(\tilde{p}''\tilde{p}''' + 6\tilde{p}'\tilde{p}^{\mathrm{iv}}), \quad p_8 = \tilde{p}^{\mathrm{iv}} - 6\tilde{p}''^2 - 6\tilde{p}'\tilde{p}''',$$

$$p_9 = 3\tilde{p}''' + 2\frac{\tilde{\theta}''^3}{\tilde{\theta}'^3}, \quad p_{10} = -2(\tilde{\theta}''^2 + \tilde{\theta}'\theta'''\tilde{p}') - 4\tilde{\theta}'\tilde{\theta}''\tilde{p}'' - \tilde{\theta}'^2\tilde{p}'''$$

where $\tilde{\theta}$, $\tilde{\theta}'$ and $\tilde{\theta}''$ can be computed with the quadratic shape functions once the numerical values of $\tilde{\theta}$ at the grid points are obtained in each iteration. The derivatives of the shape functions, $N_1'$, $N_2'$, $N_3'$ and $N_1''$, $N_2''$, $N_3''$ can be computed from Equation (35). It is worthwhile to note that the special feature of this method is that the high-order derivatives of the unknown function $\tilde{p}$ are expressed exactly or analytically in terms of lower-order derivatives, and as many as required derivatives of the unknown function $\tilde{p}$ can be obtained analytically without any difficulty.

Accordingly, the Jacobian matrix can be established.

$$J = \begin{bmatrix} 1 - g_{11}\dfrac{\mathrm{d}\tilde{p}_1}{\mathrm{d}\tilde{\theta}_1} & -g_{12}\dfrac{\mathrm{d}\tilde{p}_2}{\mathrm{d}\tilde{\theta}_2} & -g_{13}\dfrac{\mathrm{d}\tilde{p}_3}{\mathrm{d}\tilde{\theta}_3} & \cdots & -g_{1,2N+1}\dfrac{\mathrm{d}\tilde{p}_{2N+1}}{\mathrm{d}\tilde{\theta}_{2N+1}} \\ -g_{21}\dfrac{\mathrm{d}\tilde{p}_1}{\mathrm{d}\tilde{\theta}_1} & 1 - g_{22}\dfrac{\mathrm{d}\tilde{p}_2}{\mathrm{d}\tilde{\theta}_2} & -g_{23}\dfrac{\mathrm{d}\tilde{p}_3}{\mathrm{d}\tilde{\theta}_3} & \cdots & -g_{2,2N+1}\dfrac{\mathrm{d}\tilde{p}_{2N+1}}{\mathrm{d}\tilde{\theta}_{2N+1}} \\ -g_{31}\dfrac{\mathrm{d}\tilde{p}_1}{\mathrm{d}\tilde{\theta}_1} & g_{32}\dfrac{\mathrm{d}\tilde{p}_2}{\mathrm{d}\tilde{\theta}_2} & 1 - g_{33}\dfrac{\mathrm{d}\tilde{p}_3}{\mathrm{d}\tilde{\theta}_3} & \cdots & -g_{3,2N+1}\dfrac{\mathrm{d}\tilde{p}_{2N+1}}{\mathrm{d}\tilde{\theta}_{2N+1}} \\ \vdots & \vdots & \vdots & \vdots & \vdots \\ -g_{2N+1,1}\dfrac{\mathrm{d}\tilde{p}_1}{\mathrm{d}\tilde{\theta}_1} & -g_{2N+1,2}\dfrac{\mathrm{d}\tilde{p}_2}{\mathrm{d}\tilde{\theta}_2} & g_{2N+1,3}\dfrac{\mathrm{d}\tilde{p}_3}{\mathrm{d}\tilde{\theta}_3} & \cdots & 1 - g_{2N+1,2N+1}\dfrac{\mathrm{d}\tilde{p}_{2N+1}}{\mathrm{d}\tilde{\theta}_{2N+1}} \end{bmatrix} \tag{42}$$

In these computations, the numerical value of $\tilde{p}_i$ at each grid point is initially set to zero, i.e. there is no elevation of the free surface in the initial stage of the computation. The numerical

 

values of the function $\tilde{\theta}$ at the grid points on the free surface are thus computed. Then, the function $\tilde{p}$ at the grid points on the free surface is obtained from either the integral method or the differential method introduced previously, and the functions $\mathrm{d}\tilde{p}/\mathrm{d}\phi_f$ and $\mathrm{d}\tilde{p}/\mathrm{d}\tilde{\theta}$ are evaluated from Equations (31) and (38) respectively. Based on Equation (37), a subroutine, namely LMDER1 from MINPACK[2] of the NETLIB, is adopted to update the numerical values of the function $\tilde{\theta}$ at the grid points on the free surface until convergence.

For most cases, this subroutine produces a converged solution in the computation. The typical rates of convergence of the numerical solutions with the Levenberg–Marquardt algorithm are shown in Figures 9 and 14 in Section 5.

*4.2.2. Bottom geometry*. If the polygonal shape of the bottom in the $z$-plane is given (see Figure 4), based on its side lengths, $l_1, l_2, \ldots, l_{N_\alpha - 1}$, the locations of the corresponding points $a_2, a_3, \ldots, a_{N_\alpha - 1}$ in the $\bar{F}$-plane to the vertices. $A_2, A_3, \ldots, A_{N_\alpha - 1}$ may be assumed as shown in Figure 6 at the beginning of the computation. Bearing in mind that the first vertex $A_1$ maps to $a_1 = 0$ on the $\phi_b$-axis in the $\bar{F}$-plane.

With the locations of $a_1, a_2, \ldots, a_{N_\alpha - 1}$ and the angles, $\alpha_1, \alpha_2, \ldots, \alpha_{N_\alpha}$, of the polygonal surface in the $z$-plane, a system of non-linear equations of $\tilde{\theta}$ and $\tilde{p}$ on the free surface in the $\bar{F}$-plane (see Equation (37)) can be established and solved by the Levenberg–Marquardt algorithm. Once the variables $\tilde{\theta}$ and $\tilde{p}$ on the free surface in the $\bar{F}$-plane are determined, the variable $\tilde{p}$ along the bottom $\phi_b$ in the $\bar{F}$-plane can be computed from a discretized form of Equation (27). With the numerical values of both $\tilde{\theta}$ and $\tilde{p}$ at the grid points along the $\phi_b$-axis, the mapping function $z(\phi_b, 0)$ shown in Equation (43), which maps the $\phi_b$-axis in the $\bar{F}$-plane to the bottom shape in the $z$-plane, can be evaluated.

$$z(\phi_b, 0) = c + \int_{-\infty}^{\phi_b} \mathrm{e}^{\tilde{p}(t) + \mathrm{i}\tilde{\theta}(t)}\, \mathrm{d}t \tag{43}$$

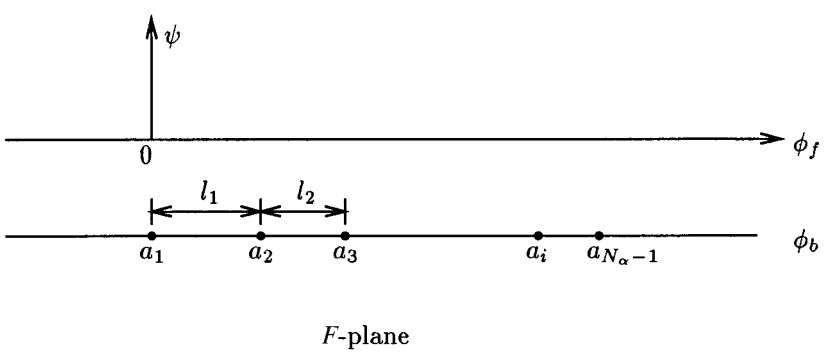


Figure 6. Initial locations of $a_i$ in the $\bar{F}$-plane.

[2] Freely available at ftp://netlib.att.com/netlib/minpack

 

Therefore, the locations of the vertices $A'_1, A'_2, \ldots, A'_{N_\alpha}$ of the bottom shape produced by the mapping function $z(\phi_b, 0)$ can be determined. The new locations, $a'_1, a'_2, \ldots, a'_{N_\alpha - 1}$, of the points, $a_1, a_2, \ldots, a_{N_\alpha - 1}$, on the $\phi_b$-axis can be thus determined from the side length ratios of the two sets of vertices $A'_1, A'_2, \ldots, A_{N_\alpha - 1}$, and $A_1, A_2, \ldots, A_{N_\alpha - 1}$

$$a'_i = a'_1 + \sum_{k=1}^{i-1} (a_{k+1} - a_k) \frac{l_k}{l'_k}, \quad \text{for } i = 2, 3, \ldots, N_\alpha - 1 \tag{44}$$

where $l_k$ and $l'_k$ are the distances between vertices $A_k$ and $A_{k+1}$, and $A'_k$ and $A_{k+1}$ respectively. It is noted that $a'_1 = 0$.

The whole process is repeated until the locations of $a'_2, a'_3, \ldots$ and $a'_{N_\alpha - 1}$ converge.

## 5. EXAMPLES

To test the numerical scheme developed in this research, three examples of supercritical flow past polygonal obstructions are computed. The first example is taken from References [2,4] for comparing the current numerical results with those of other researchers. The second example is to test the sensitivity of the current computer code with respect to unsymmetrical triangular obstructions, and the third example is a supercritical flow over a ramp with two different heights and five different inclining angles, which is seldom dealt with in the published literature. The elevations of the free surface as well as the pressure distributions along the polygonal bottom are presented for these examples.

### *5.1. Example 1: supercritical flow over symmetric obstruction*

In this example, three different cases of a supercritical flow past a symmetric triangular obstruction, as shown in Figure 7, for two Froude numbers, $F_n = \sqrt{10}$ and 2, are computed.

In the computation, the free surface of the midstream ($-10 < \phi_f < 10$) in the $\bar{F}$-plane is discretized into 100 elements. Typically, a converged solution is obtained within 100 iterations with a root-mean-square (r.m.s.) difference (see below) of $10^{-13}$ for a set of $a_i$, $i = 1$, 2 and 3, in the $\bar{F}$-plane (which are the corresponding points of the vertices $A_1$, $A_2$ and $A_3$ of the triangular obstruction in the $z$-plane). About ten iterations are required to obtain the desired location of the vertices at the bottom in the $z$-plane with a relative error of $10^{-5}$. For

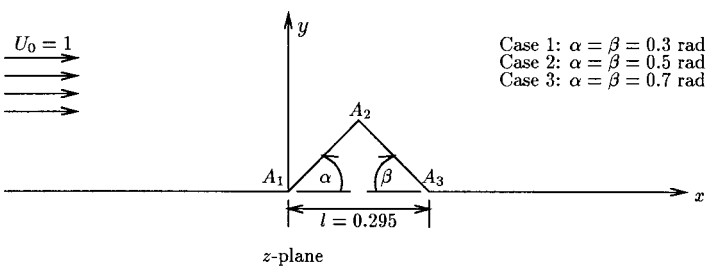


Figure 7. Supercritical flow over a triangular obstruction.

 

$F_n = \sqrt{10}$, a comparison of the current numerical results with those of Boutros *et al.* [2] and King *et al.* [4] for the elevation of free surface above the obstruction is shown in Figure 8. Evidently, the current results for $\alpha = 0.3$ are in agreement with those of King *et al.* A typical rate of convergence with the Levenberg–Marquardt algorithm is shown in Figure 9, where the r.m.s. difference is defined as

$$\text{r.m.s.} = \frac{1}{2N+1}\sqrt{\sum_{i=1}^{2N+1} I_i^2} \tag{45}$$

where $I_i$ is defined in Equation (37) and $2N+1$ is the number of grid points distributed on the free surface.

Due to the symmetrical nature of the triangular obstruction, the current numerical results are more reasonable than those of Boutros *et al.* The pressure distributions along the arc length of the bottom for these three cases are shown in Figure 10. It can be seen that the pressure at the tip of the triangular obstruction tends to $-\infty$ as the height of the triangular obstruction increases and because of the symmetrical distribution of the pressure, there is no net force acting on the triangular obstruction. Figure 11 shows the computational results of the free surface elevations along the arc length of the bottom for $F_n = 2$.

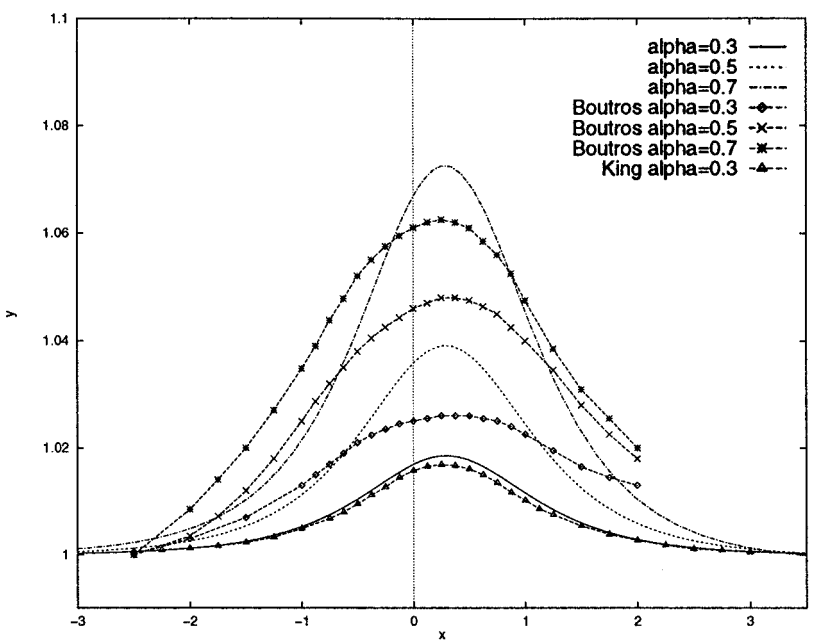


Figure 8. Free surface elevation for $F_n = \sqrt{10}$, $\alpha = \beta$ and $l = 0.59$.

 

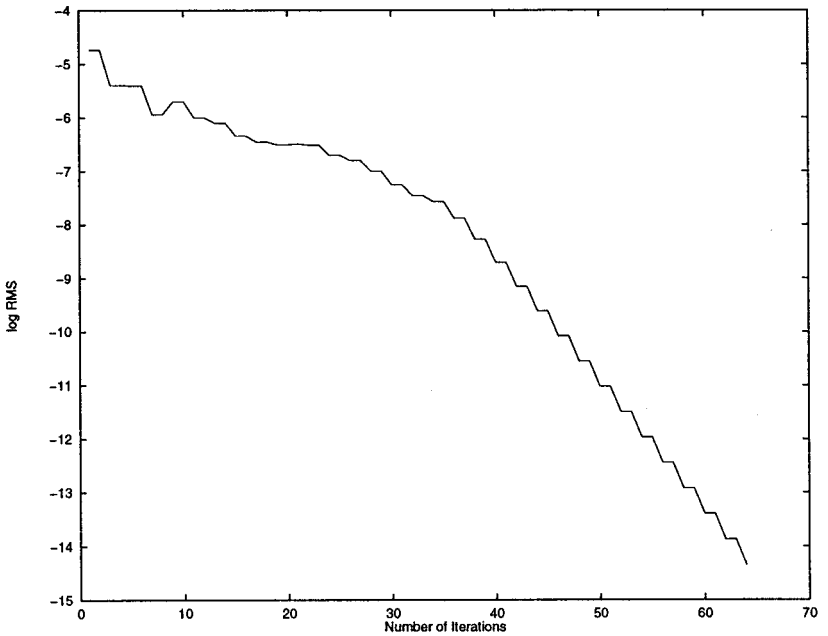


Figure 9. Typical rate of convergence of Example 1 ($\alpha = 0.3$).

### 5.2. Example 2: supercritical flow over unsymmetric obstruction

In this example, five different cases of a supercritical flow past an unsymmetric triangular obstruction similar to the configuration of the first example for $F_n = \sqrt{10}$ are considered. Length $l$ and angle $\alpha$ of the triangular obstruction are fixed and chosen to be 0.12930913 and 0.3 rad respectively. Five different heights of the triangular obstructions as shown in Table I are computed. The free surface of the midstream ($-10 < \phi_f < 10$) in the $\bar{F}$-plane is discretized into 100 elements. Typically, a converged solution is also obtained within 100 iterations with an r.m.s. difference (see below) of $10^{-13}$ for a set of $a_i$, $i = 1,2$ and 3, in the $\bar{F}$-plane. About ten iterations are required to obtain the desired location of the vertices at the bottom in the $z$-plane with a relative error of $10^{-5}$. Figure 12 shows the computational results of the free surface elevations along the arc length of the bottom for each case.

### 5.3. Example 3: supercritical flow over a ramp

The third example computes a supercritical flow over a ramp with two different heights, $h = 0.4$ and 0.6, and six different angles, $\alpha = 15°$, 30°, 45°, 60°, 75° and 90° as show n in Figure 13 for Froude number $F_n = \sqrt{10}$.

Similar to the previous example, 100 quadratic elements are used to discretize the free surface ($-16 < \phi_f < 16$) in the $\bar{F}$-plane. A converged solution is obtained within about 100

 

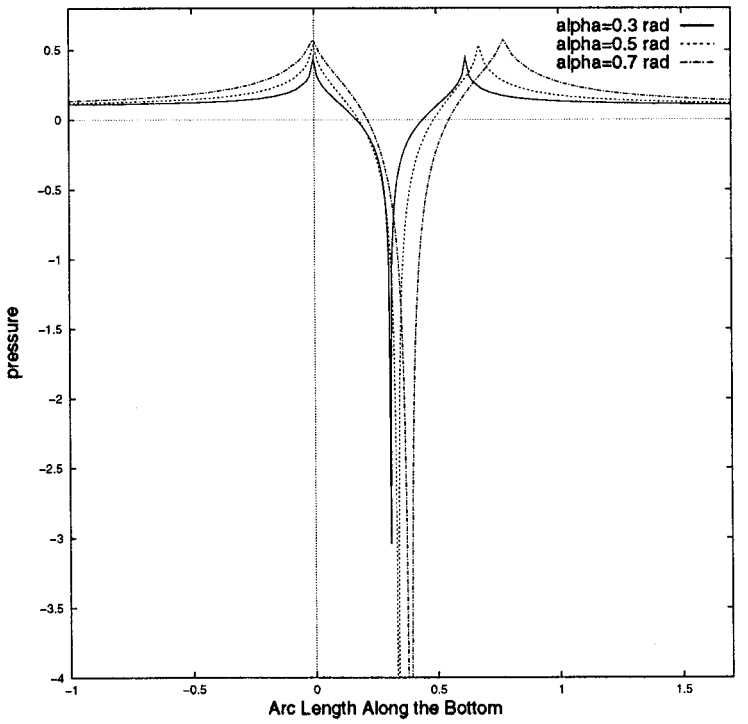


Figure 10. Pressure distribution along the arc length of the bottom for $F_n = \sqrt{10}$.

iterations with an r.m.s. of $10^{-11}$ for a set of $a_1$ and $a_2$ in the $\bar{F}$-plane (which are the corresponding points of the vertices $A_1$ and $A_2$ of the ramp in the $z$-plane). About 15 iterations are required to obtain the desired location of the vertices in the physical domain with a relative error of $10^{-5}$. A typical rate of convergence is shown in Figure 14, which is for the case of $h = 0.4$ and $\alpha = 45°$.

The numerical results of the elevations of the free surface for $h = 0.4$ and 0.6 are shown in Figures 15 and 16 respectively.

Based on the number of iterations required for a converged numerical solution, the supercritical flow over a ramp seems to be more difficult to compute than that over a triangular obstruction. It may be due to the unsymmetric nature of the obstacle.

## 6. CONCLUSION AND REMARKS

In this research, the generalized Schwarz–Christoffel transformation associated with the Hilbert transform is employed successfully to solve the supercritical flow over polygonal obstructions. The excellent convergence shown in Figures 9 and 14 confirms that the boundary

 

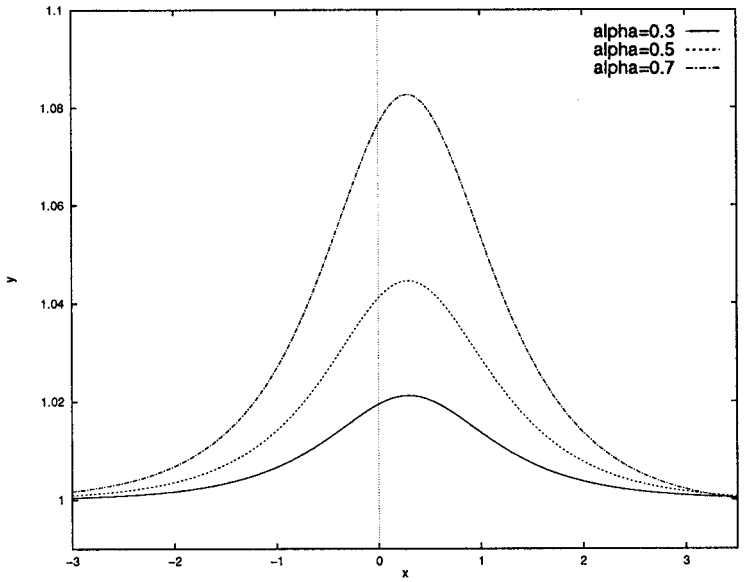


Figure 11. Free surface elevation for $F_n = 2$, $\alpha = \beta$ and $l = 0.59$.

Table I. Angles and lengths for Example 2.

| Case No. | $\alpha$ (rad) | $h$ | $\beta$ (rad) |
|---|---|---|---|
| 1 | 0.30 | 0.010 | 0.102748952 |
| 2 | 0.30 | 0.015 | 0.183513514 |
| 3 | 0.30 | 0.020 | 0.300000000 |
| 4 | 0.30 | 0.025 | 0.476018198 |
| 5 | 0.30 | 0.030 | 0.748075597 |

integral equation and the free surface condition shown in Equations (28) and (31), are satisfied almost exactly at all grid points on the $\phi_f$-axis in the $\bar{F}$-plane. A typical numerical value for the pressure on the free surface is in the order of $10^{-7}$.

From numerical experiments, it shows that

1. the differential and integral methods developed in Section 4 for treating the free surface condition produce almost the same numerical results for the variables $\tilde{p}$ and $\tilde{\theta}$ on the free surface in the standard domain. Since there is a log term in the integral method, the differential method may be more versatile for dealing with different types of non-linear free surface problems;
2. through additional computations with 200 and 300 grid points distributed on the free surface, the convergences of the numerical solution are almost the same as that shown in Section 5, which verifies the numerical scheme developed in this paper is grid-independent.

 

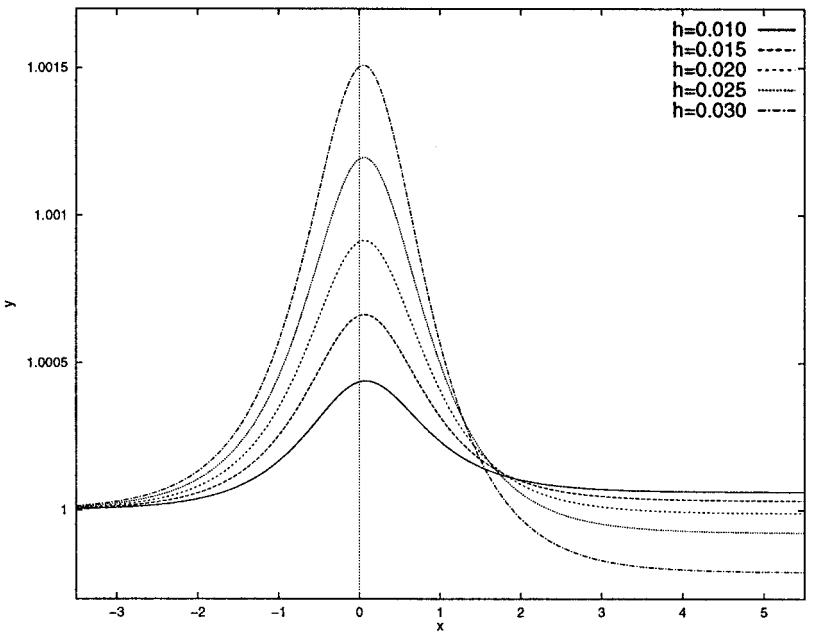


Figure 12. Free surface elevation for $F_n = \sqrt{10}$, $\alpha = 0.3$ and $l = 0.12930913$.

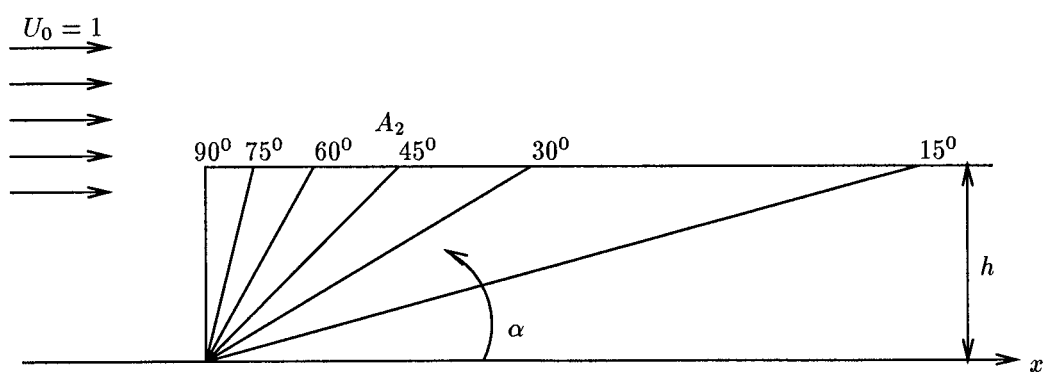


Figure 13. Configuration of the ramp.

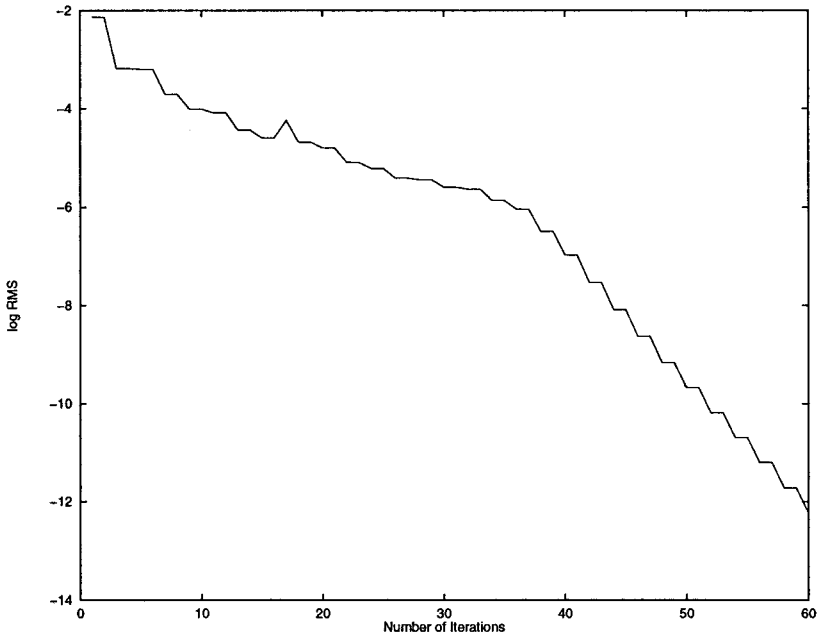


Figure 14. Rate of convergence for $h = 0.4$, $\alpha = 45°$.

Also noted in this numerical scheme was that the standard domain is not truncated. The only assumptions made are that

1. The numerical values of $\tilde{p}$ and $\tilde{\theta}$ from $-\infty$ to the first grid point in the midstream are the same as those at the first grid point.
2. Similarly, the numerical values of $\tilde{p}$ and $\tilde{\theta}$ from the last grid point in the midstream to $\infty$ are the same as those at the last grid point.

The second assumption is not applicable to the sub-critical flow due to the fact that the waves will be generated in the downstream.

To validate the computational results of the discretized integral equation, the sum of each row in the $g$ matrix in Equation (36) can also be computed and should be almost equal to 0. This is because the sum of each row in the $g$ matrix is identical to

$$-\int_{-\infty}^{\infty} \frac{1}{2\sinh\dfrac{\pi}{2}(\phi_f - s_f)}\,\mathrm{d}s_f = -\log 1 = 0 \tag{46}$$

It is independent of the location of the field point $\phi_f$ on the free surface in the midstream. Similarly, if the physical domain has a curved solid boundary, the first integral in Equation (28) has to be discretized as mentioned in Section 4.1, and the sum of each row in the $h$ matrix has to be approximately equal to 1, which is the value obtained from the exact integral of

 

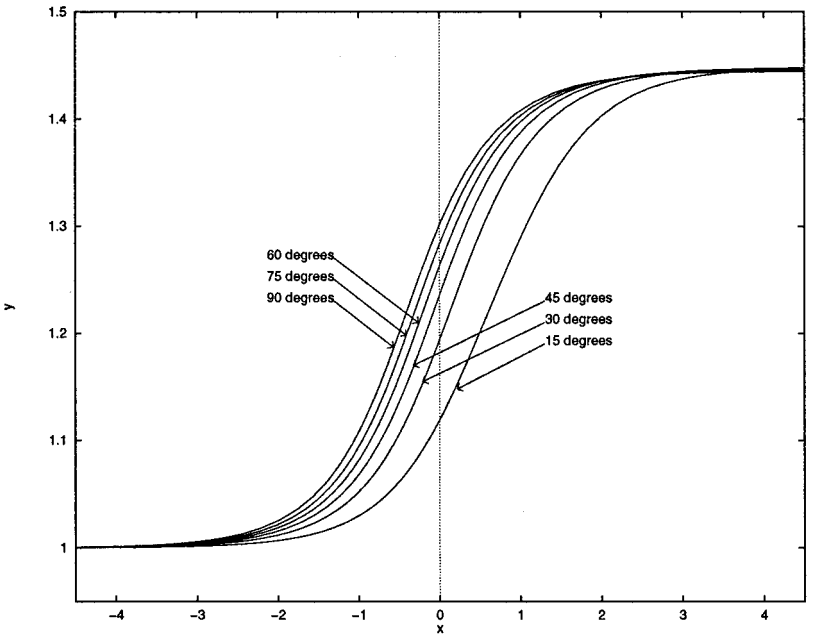


Figure 15. Supercritical flow over a ramp of $F_n = \sqrt{10}$, $h = 0.4$.

$$\int_{-\infty}^{\infty} \frac{1}{2\cosh\dfrac{\pi}{2}(\phi_f - s_b)}\,\mathrm{d}s_b = -\frac{1}{\pi}\left[\tan^{-1}(-\infty) - \tan^{-1}\infty\right] = 1 \tag{47}$$

For low Froude numbers, such as $1 < F_n < 2$, a converged solution of the discretized integral equation (36) becomes sensitive to the grid distribution on the free surface in the standard domain. This is caused by the discontinuity of the derivatives of the quadratic shape functions $N_i$, $i = 1, 2, 3$, used by the variable $\tilde{\theta}$ at the grid points where $\mathrm{d}\tilde{\theta}/\mathrm{d}\phi_f \approx 0$ and $\mathrm{d}\tilde{p}/\mathrm{d}\tilde{\theta} \to \infty$, which is required to evaluate the Jacobian matrix for solving non-linear equations. Therefore, the cubic spline shape functions with continuous first and second derivatives at each grid points on the free surface are recommended for the low Froude numbers.

Due to the flexibility of the discretization technique for the boundary integral equation associated with the differential method to impose the free surface condition, the numerical scheme proposed in this research can be applied to solve a variety of two-dimensional fully non-linear free surface flow problems in the engineering field, such as waterfalls, weir flows and wave–body interactions. Furthermore, the orthogonal numerical grids generated from the solution of the non-linear free surface flow can be used to solve a viscous flow problem with a free surface.

 

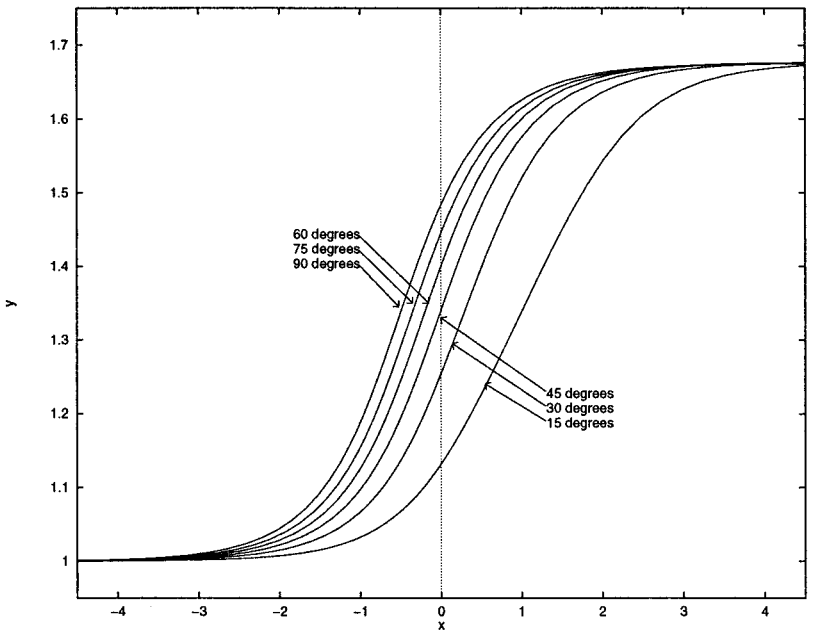


Figure 16. Supercritical flow over a ramp of $F_n = \sqrt{10}$, $h = 0.6$.

ACKNOWLEDGMENTS

The author would like to thank Dr Julio Militzer for his helpful comments.

## APPENDIX A. NUMERICAL COMPUTATION OF SINGULAR INTEGRALS

1. If $i = 1$, $g(i, i)$ is expressed in the form

$$g(1,1) = -\int_{-\infty}^{s_{f_1}} \frac{1}{2\sinh\frac{\pi}{2}(s_{f_1} - s_f)}\,\mathrm{d}s_f - \int_{s_{f_1}}^{s_{f_2}} \frac{N_1(\gamma(s_f))}{2\sinh\frac{\pi}{2}(s_{f_1} - s_f)}\,\mathrm{d}s_f$$

$$= -\int_{s_{f_1}}^{s_{f_2}} \frac{N_1(\gamma(s_f)) - 1}{2\sinh\frac{\pi}{2}(s_{f_1} - s_f)}\,\mathrm{d}s_f - P.V.\int_{-\infty}^{s_{f_2}} \frac{1}{2\sinh\frac{\pi}{2}(sf_1 - s_f)}\,\mathrm{d}s_f \tag{48}$$

When $s_f \to s_{f_1}$, the limiting value of the integrand in the first integral on the right-hand side is

 

$$\lim_{s_f \to s_{f_1}} \frac{N_1(\gamma(s_f)) - 1}{2 \sinh \dfrac{\pi}{2}(s_{f_1} - s_f)} = \frac{3}{\pi(s_{f_2} - s_{f_1})} \tag{49}$$

The second integral on the right-hand side can be carried out analytically as follows:

$$P.V. \int_{-\infty}^{s_{f_2}} \frac{1}{2 \sinh \dfrac{\pi}{2}(s_{f_1} - s_f)} \, \mathrm{d}s_f = -\frac{1}{\pi} \log\left[ \tanh \frac{\pi}{4}(s_{f_2} - s_{f_1}) \right] \tag{50}$$

As a result, $g(1, 1)$ is reduced to

$$g(1, 1) = -\int_{s_{f_1}}^{s_{f_2}} \frac{N_1(\gamma(s_f)) - 1}{2 \sinh \dfrac{\pi}{2}(s_{f_1} - s_f)} \, \mathrm{d}s_f + \frac{1}{\pi} \log\left[ \tanh \frac{\pi}{4}(s_{f_2} - s_{f_1}) \right] \tag{51}$$

2. If $i = 3, 5, 7, \ldots, 2N - 1$ (odd number), $g(i, i)$ is given by

$$\begin{aligned} g(i, i) &= -\int_{s_{f_{j-1}}}^{s_{f_j}} \frac{N_3(\gamma(s_f))}{2 \sinh \dfrac{\pi}{2}(s_{f_1} - s_f)} \, \mathrm{d}s_f - \int_{s_{f_j}}^{s_{f_{j+1}}} \frac{N_1(\gamma(s_f))}{2 \sinh \dfrac{\pi}{2}(s_{f_1} - s_f)} \, \mathrm{d}s_f \\ &= -\int_{s_{f_{j-1}}}^{s_{f_j}} \frac{N_3(\gamma(s_f)) - 1}{2 \sinh \dfrac{\pi}{2}(s_{f_j} - s_f)} \, \mathrm{d}s_f - \int_{s_{f_j}}^{s_{f_{j+1}}} \frac{N_1(\gamma(s_f)) - 1}{2 \sinh \dfrac{\pi}{2}(s_{f_j} - s_f)} \, \mathrm{d}s_f \\ &\quad - P.V. \int_{s_{f_{j-1}}}^{s_{f_{j+1}}} \frac{1}{2 \sinh \dfrac{\pi}{2}(s_{f_j} - s_f)} \, \mathrm{d}s_f \end{aligned} \tag{52}$$

When $s_f \to s_{f_j}$, the limiting values of the integrand in the first and second integrals on the right-hand side can be easily derived as

$$\lim_{s_f \to s_{f_j}} \frac{N_3(\gamma(s_f)) - 1}{2 \sinh \dfrac{\pi}{2}(s_{f_j} - s_f)} = -\frac{3}{\pi(s_{f_{j-1}} - s_{f_j})}$$

$$\lim_{s_f \to s_{f_j}} \frac{N_1(\gamma(s_f)) - 1}{2 \sinh \dfrac{\pi}{2}(s_{f_j} - s_f)} = \frac{3}{\pi(s_{f_{j+1}} - s_{f_j})}$$

The last integral on the right-hand side of Equation (52) can be carried out analytically,

 

$$P.V.\int_{s_{f_{j-1}}}^{s_{f_{j+1}}}\frac{1}{2\sinh\dfrac{\pi}{2}(s_{f_j}-s_f)}\,\mathrm{d}s_f=-\frac{1}{\pi}\log\left[\frac{\tanh\dfrac{\pi}{4}(s_{f_{j+1}}-s_{f_j})}{\tanh\dfrac{\pi}{4}(s_{f_j}-s_{f_{j-1}})}\right] \tag{53}$$

Consequently, $g(i,i)$ becomes

$$g(i,i)=-\int_{s_{f_{j-1}}}^{s_{f_j}}\frac{N_3(\gamma(s_f))-1}{2\sinh\dfrac{\pi}{2}(s_{f_j}-s_f)}\,\mathrm{d}s_f-\int_{s_{f_j}}^{s_{f_{j+1}}}\frac{N_1(\gamma(s_f))-1}{2\sinh\dfrac{\pi}{2}(s_{f_j}-s_f)}\,\mathrm{d}s_f$$
$$+\frac{1}{\pi}\log\left[\frac{\tanh\dfrac{\pi}{4}(s_{f_{j+1}}-s_{f_j})}{\tanh\dfrac{\pi}{4}(s_{f_j}-s_{f_{j-1}})}\right] \tag{54}$$

3. If $i=2,4,6,\ldots,2N$ (even number), $g(i,i)$ takes the form of

$$g(i,i)=-\int_{s_{f_j}}^{s_{f_{j+1}}}\frac{N_2(\gamma(s_f))}{2\sinh\dfrac{\pi}{2}\left[\dfrac{1}{2}(s_{f_j}+s_{f_{j+1}})-s_f\right]}\,\mathrm{d}s_f=-\int_{s_{f_j}}^{s_{f_{j+1}}}\frac{N_2(\gamma(s_f))-1}{2\sinh\dfrac{\pi}{2}\left[\dfrac{1}{2}(s_{f_j}+s_{f_{j+1}})-s_f\right]}\,\mathrm{d}s_f$$
$$-P.V.\int_{s_{f_j}}^{s_{f_{j+1}}}\frac{1}{2\sinh\dfrac{\pi}{2}\left[\dfrac{1}{2}(s_{f_j}+s_{f_{j+1}})-s_f\right]}\,\mathrm{d}s_f \tag{55}$$

When $s_f\to\frac{1}{2}(s_{f_j}+s_{f_{j+1}})$, the limiting value of the integrand in the first integral on the right-hand side is found to be zero, i.e.

$$\lim_{s_f\to\frac{1}{2}(s_{f_j}+s_{f_{j+1}})}\frac{N_2(\gamma(s_f))-1}{2\sinh\dfrac{\pi}{2}\left(\dfrac{1}{2}(s_{f_j}+s_{f_{j+1}})-s_f\right)}=0 \tag{56}$$

The second integral on the right-hand side can be carried out analytically,

$$P.V.\int_{s_{f_j}}^{s_{f_{j+1}}}\frac{1}{2\sinh\dfrac{\pi}{2}\left(\dfrac{1}{2}(s_{f_j}+s_{f_{j+1}})-s_f\right)}\,\mathrm{d}s_f=-\frac{1}{\pi}\log\left\{\frac{\tanh\dfrac{\pi}{4}\left[s_{f_{j+1}}-\dfrac{1}{2}(s_{f_j}+s_{f_{j+1}})\right]}{\tanh\dfrac{\pi}{4}\left(\dfrac{1}{2}[(s_{f_j}+s_{f_{j+1}})-s_{f_j}]\right)}\right\} \tag{57}$$

 

Therefore, in this case, $g(i, i)$ reads

$$g(i,i) = -\int_{s_{f_j}}^{s_{f_{j+1}}} \frac{N_2(\gamma(s_f)) - 1}{2\sinh\dfrac{\pi}{2}\left[\dfrac{1}{2}(s_{f_j} + s_{f_{j+1}}) - s_f\right]}\,\mathrm{d}s_f \tag{58}$$

4. If $i = 2N+1$, $g(i, i)$ is expressed as

$$\begin{aligned} g(2N+1, 2N+1) &= -\int_{s_{f_N}}^{s_{f_{N+1}}} \frac{N_3(\gamma(s_f))}{2\sinh\dfrac{\pi}{2}(s_{f_{N+1}} - s_f)}\,\mathrm{d}s_f - \int_{s_{f_{N+1}}}^{\infty} \frac{1}{2\sinh\dfrac{\pi}{2}(s_{f_{N+1}} - s_f)}\,\mathrm{d}s_f \\ &= -\int_{s_{f_N}}^{s_{f_{N+1}}} \frac{N_3(\gamma(s_f)) - 1}{2\sinh\dfrac{\pi}{2}(s_{f_{N+1}} - s_f)}\,\mathrm{d}s_f - P.V.\int_{s_{f_N}}^{\infty} \frac{1}{2\sinh\dfrac{\pi}{2}(s_{f_{N+1}} - s_f)}\,\mathrm{d}s_f \end{aligned} \tag{59}$$

When $s_f \to s_{f_{N+1}}$, the limiting value of the integrand in the first integral on the right-hand side is shown in Equation (60),

$$\lim_{s_f \to s_{f_1}} \frac{N_3(\gamma(s_f)) - 1}{2\sinh\dfrac{\pi}{2}(s_{f_{N+1}} - s_f)} = -\frac{3}{\pi(s_{f_{N+1}} - s_{f_N})} \tag{60}$$

The second integral on the right-hand side, as usual, can be carried out analytically,

$$P.V.\int_{s_{f_N}}^{\infty} \frac{1}{2\sinh\dfrac{\pi}{2}(s_{f_1} - s_f)}\,\mathrm{d}s_f = \frac{1}{\pi}\log\left[\tanh\frac{\pi}{4}(s_{f_{N+1}} - s_{f_N})\right] \tag{61}$$

Hence, $g(i, i)$ becomes

$$g(N+1, N+1) = -\int_{s_{f_N}}^{s_{f_{N+1}}} \frac{N_3(\gamma(s_f)) - 1}{2\sinh\dfrac{\pi}{2}(s_{f_{N+1}} - s_f)}\,\mathrm{d}s_f - \frac{1}{\pi}\log\left[\tanh\frac{\pi}{4}(s_{f_{N+1}} - s_{f_N})\right] \tag{62}$$

## REFERENCES


1. Lamb H. *Hydrodynamics*, 6th edn. Dover: New York, 1945.
2. Boutros YZ, Abd-el-Malek MB, Masoud SZ. Hilbert method for numerical solution of flow from a uniform channel over irregular bottom topographies. *Computational Methods in Applied Mechanics and Engineering* 1987; **65**: 215–228.
3. Dias F, Vanden-Broeck JM. Open channel flow with submerged obstruction. *Journal of Fluid Mechanics* 1989; **206**: 155–170.

4. King AC, Bloor MIG. Free-surface flow of a stream obstructed by an arbitrary bed topography. *Quarterly Journal of Mechanics and Applied Mathematics* 1990; **43**: 87–106.
5. Li YF, Chuang JM, Hsiung CC. *Computation of non-linear 2D free-surface flow using the Hilbert methods*. 6th International Workshop on Water Waves and Floating Bodies, Woods Hole, MA, April 1991.
6. Abd-el-Malek MB, Hanna SN. Approximate solution of gravity flow from a uniform channel over triangular bottom for large Froude number. *Applied Mathematical Modelling* 1991; **15**: 25–32.
7. Hanna SN, Abdel-Malek MN, Abd-el-Malek MB. Super-critical free-surface flow over a trapezoidal obstacle. *Journal of Computational and Applied Mathematics* 1996; **66**: 279–293
8. King AC, Bloor MIG. Free-surface flow over a step. *Journal of Fluid Mechanics* 1987; **182**: 193–208.
9. Frobe LK, Schwartz LM. Free-surface flow over a semi-circular obstruction. *Journal of Fluid Mechanics* 1982; **114**: 288–314.
10. Forbes LK. Critical free-surface flow over a semi-circular obstruction. *Journal of Engineering Mathematics* 1988; **22**: 3–13.
11. Chow WL, Tan T. Inviscid solution for the problem of free overfall. *Journal of Applied Mechanics* 1979; **46**: 1–5.
12. Naghidi, PM, Rubin MB. On inviscid flow in waterfall. *Journal of Fluid Mechanics* 1981; **103**: 375–387.
13. Smith AC, Abd-el-Malek MB. Hilbert's method for numerical solution of flow from a uniform channel over a shelf. *Journal of Engineering Mathematics* 1983; **17**: 27–39.
14. Goh KHM, Tuck EO. Thick waterfalls from horizontal slots. *Journal of Engineering Mathematics* 1985; **19**: 341–349.
15. Abd-el-Malek MB. Flow in a waterfall with large Froude number. *Journal of Computational and Applied Mathematics* 1994; **50**: 87–98.
16. Meiron DI, Orszag SA. Applications of numerical conformal mapping. *Journal of Computers in Physics* 1981; **40**: 345–360.
17. Li YF, Chuang JM, Hsiung CC. *Numerical solution of nonlinear wave–body interactions using numerical conformal mapping*. 7th International Workshop on Water Wave and Floating Bodies, France, May 1992.
18. Vanden-Broeck JM, Keller JB. Weir flows. *Journal of Fluid Mechanics* 1987; **176**: 283–293.
19. Dias F, Elcrat AR, Trefethen LN. Ideal jet flow in two dimensions. *Journal of Fluid Mechanics* 1987; **185**: 275–288.
20. Tuck EO. Efflux from a slit in a vertical wall. *Journal of Fluid Mechanics* 1987; **176**: 253–264.
21. Dias F, Elcrat AR. Ideal jet flow with a stagnation streamline. *European Journal of Mechanics*, *B. Fluids* 1992; **11**: 233–247.
22. Floryan JM, Zemach C. Schwarz–Christoffel mappings: a general approach. *Journal of Computational Physics* 1987; **72**: 347–371.
23. Chuang JM. *Mathematical formulation of the generalized Schwarz–Christoffel transformation: part I*. 5th International Congress on Computational and Applied Mathematics (ICCAM 92), Leuven, Belgium, 1992.
24. More J. The Levenberg–Marquardt algorithm, implementation and theory, numerical analysis. In *Lecture Notes in Mathematics 630*, Watson GA (ed). Springer: Berlin, 1977.

 